Supporting Information

Thiazole-Based Scaffolding for High Performance Solar Cells

Ibrahim Bulut,[a] Patricia Chávez,[a] Antoine Mirloup,[b] Quentin Huaulmé,[b] Anne Hébraud,[a] Benoît Heinrich,[c] Sadiara Fall,[d] Stéphane Méry,[c] Raymond Ziessel,[b] Thomas Heiser,[d] Patrick Lévêque,[d]* Nicolas Leclerc[a]*

[a] Institut de Chimie et Procédés pour l'Energie, l'Environnement et la Santé (ICPEES), Département d'Ingénierie Polymère, UMR 7515 Université de Strasbourg-CNRS, 25 rue Becquerel, Strasbourg 67087, France.
E-mail: leclercn@unistra.fr
[b] Institut de Chimie et Procédés pour l'Energie, l'Environnement et la Santé (ICPEES), Laboratoire de Chimie Moléculaire et Spectroscopies Avancées, UMR 7515 Université de Strasbourg-CNRS, 25 rue Becquerel, Strasbourg 67087, France.
[c] Institut de Physique et Chimie des Matériaux de Strasbourg (IPCMS), UMR 7504 Université de Strasbourg-CNRS 23 rue du Loess, Strasbourg 67034, France.
[d] Laboratoire des sciences de l'ingénieur, de l'informatique et de l'imagerie (ICube), UMR 7357 Université de Strasbourg-CNRS 23 rue du Loess, Strasbourg 67037, France.
E-mail: patrick.leveque@unistra.fr

Experimental Section

XRD Measurements.

Powder XRD patterns were obtained with a linear monochromatic Cu Kα1 beam (λ = 1.5405 Å) obtained using a sealed-tube generator equipped with a bent quartz monochromator and a curved Inel CPS 120 counter gas-filled detector; periodicities up to 70 Å can be measured, and the sample temperature controlled to within ±0.01 °C from 20 to 200 °C. The sample was filled in Lindemann capillaries and exposure times were of 6 h.

GIWAXS Measurements.

GIWAXS measurements were conducted at PLS-II 9A U-SAXS beamline of Pohang Accelerator Laboratory (PAL) in Korea, on films deposited by spin-coating on silicon wafer (identical deposition processes to the active layers solar cells). The X-rays coming from the

vacuum undulator (IVU) were monochromated using Si(111) double crystals and focused on the detector using K-B type mirrors. Patterns were recorded with a 2D CCD detector (Rayonix SX165). The sample-to-detector distance was about 225 mm for an energy of 11.08 keV (1.119 Å).

Field effect mobility measurements.

Bottom contact organic field-effect transistors (OFETs) were elaborated on commercially available pre-patterned test structures whose source and drain contacts were composed of a 30 nm thick gold layer on top of a 10 nm thick Indium Tin Oxide (ITO) layer. A 230 nm thick silicon oxide was used as the gate dielectric and an n-doped ($3x10^{17}/cm^3$) silicon crystal as the gate electrode. The channel length and channel width were 20 µm and 10 mm, respectively. The test structures were cleaned in acetone and isopropyl alcohol and subsequently in an ultra-violet ozone system for 30 minutes. Then, hexamethyldisilazane (HMDS) was spin-coated (500 rpm for 5 s and then 4000 rpm for 50 s) under nitrogen ambient followed by an annealing step at 130°C for 10 minutes. Finally, 5 mg/mL anhydrous chloroform of dye solutions were spin coated (1250 rpm for 60 s and 2250 rpm for 60 s) to complete the FET devices. The samples were then left overnight under vacuum ($<10^{-6}$ mbar) to remove residual solvent traces. Both, the FET elaboration and characterizations were performed in nitrogen ambient. The transistor output and transfer characteristics were recorded using a Keithley 4200 semiconductor characterization system. The charge carrier mobility was extracted in the saturation regime using the usual formalism on FET devices annealed at the same temperature as the optimized photovoltaic devices.

Space Charge Limited Current (SCLC) devices preparation

Hole-only SCLC devices were elaborated to investigate the out-of-plane mobility. The device structure was the following: ITO/PEDOT:PSS/small molecule/PEDOT:PSS/MoO_3/Ag. Highly conductive poly(3,4-ethylenedioxythiophene):polystyrene-sulfonate (PEDOT:PSS)

was used as hole injection electrode. Indium tin oxide (ITO) coated glass with a sheet resistance of 20 Ω/sq was used as substrate. The ITO layer was cleaned sequentially by ultrasonic treatments in acetone, isopropyl alcohol and deionized water. After an additional 30 minutes exposure to ultra-violet generated ozone, a 40 nm thick PEDOT:PSS layer was spin-coated from an aqueous solution on top of the ITO layer and dried for 30 min at 140°C. Chloroform (TAT-TzDPP) or chlorobenzene (TAT-ThDPP) dye solutions of varying concentration were prepared and stirred at room temperature for 24h before spin-coating on top of PEDOT:PSS. The resulting dye layer thickness ranged from 75 nm to 150 nm as measured by profilometer. The devices were completed by thermal evaporation of MoO_3(7 nm)/Ag(120nm) as top electrode. Device elaboration and characterization were done at room temperature in a nitrogen-filled glove box. Several dye layer thicknesses were tested to insure that the observed deviation from Ohm low in the (I-V) characteristics was not due to injection problems.

The hole mobility is extracted using the standard expression for charge space limited current density following the Mott-Gurney law:

$$J = \frac{9}{8}\varepsilon_r \varepsilon_0 \mu_h \frac{V^2}{L^3}$$

Where ε_0 is the permittivity of free space, ε_r is the dye dielectric constant, μ_h is the hole mobility, V is the voltage drop across the device and L is the film thickness.

Photovoltaic devices preparation

Bulk heterojunction devices were elaborated using the different synthesized molecules as electron-donor and $PC_{71}BM$ as electron-acceptor. Standard solar cells were elaborated by using the following device structure: ITO/PEDOT-PSS(40nm)/electron-donor molecule:$PC_{71}BM$/Ca(20 nm)Al(120 nm). Inverted solar cells using polyethyleneimine, 80% ethoxylated (PEIE) as an interfacial layer were elaborated with the following structure: ITO/PEIE(5 nm)/electron-donor molecule:$PC_{71}BM$/MoO_3(7 nm)Ag(120 nm). Indium Tin

Oxide coated glass with a surface resistance lower than 20 Ω/sq was used as the transparent substrate. Substrates were cleaned sequentially by ultrasonic treatments in acetone, isopropyl alcohol, and deionized water. After an additional cleaning for 30 minutes under ultra-violet generated ozone, PEDOT-PSS or PEIE (M_W=70000 g/mol) were spin coated at 1500 rpm for 60s or 5000 rpm for 60s, respectively. Finally, PEDOT-PSS was thermally annealed for 30 minutes at 140°C while the PEIE thin film was thermally annealed for 10 minutes at 100°C, both under nitrogen atmosphere. The organic solvent dye:$PC_{71}BM$ solutions were stirred for at least 24 hours at 50°C before spin-coating. An extra stirring for 15 minutes at 100°C was added just before the active layer deposition. In the following are reported the best conditions leading to optimal devices for each molecule. Thus, the molecule TAT-TzDPP has been deposited from a chloroform solution at the concentration of 7 mg/mL. The molecule TAT-ThDPP has been deposited from a chlorobenzene solution at the concentration of 15 mg/mL. All molecule active layers were spin-coated in the following conditions: a first 120 seconds step (speed: 2000 rpm, acceleration: 600 rpm/s) followed by a second 60 seconds step (speed: 2500 rpm, acceleration: 600 rpm/s). A post-deposition thermal annealing process (for 10 or 15 minutes from 100 to 120°C) was added before the electrode thermal evaporation. Each device contained four 12 mm^2 diodes, the surface of each diode being carefully defined by a shadow mask. The photovoltaic cell elaboration after substrate preparation was performed in nitrogen ambient

Photovoltaic measurements.

Current density versus Voltage (J-V) characteristics were measured using a Keithley 2400 source measurement unit under darkness and under AM1.5G (100 mW/cm^2) illumination. The standard illumination was provided by a Class A Lot Oriel solar simulator (550 W filtered Xe lamp) and the illumination power was calibrated using a reference silicon solar cell. Photovoltaic measurements were also performed with different light intensities using neutral

density filters with different absorption coefficient. External Quantum Efficiency (EQE) measurements were performed using a home-made setup including a 150 W Lot Oriel Xe solar simulator as a light source, a Jobin-Yvon microHR monochromator and several focusing lenses to obtain a 2 mm diameter monochromatic light beam on the solar cell under investigation. Calibrated silicon reference cells were used to monitor the incident and the reflected light power for each wavelength. All the characterizations were performed in nitrogen ambient.

Atomic Force Microscopy (AFM) measurements.

Tapping-mode atomic force microscope (AFM) measurements were performed on a Nanoscope IIIa system commercialized by Veecor®.

Building block synthesis:

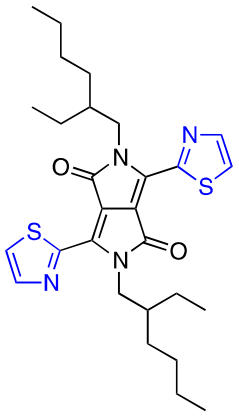

Synthesis of DPP-Tz (1): 2,5-bis(2-ethylhexyl)-3,6-di(thiazol-2-yl)pyrrolo[3,4-*c*]pyrrole-1,4(2*H*,5*H*)-dione[S1]

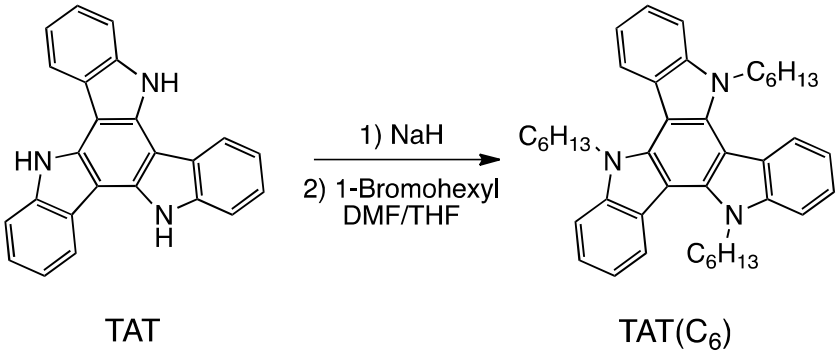

TAT TAT(C_6)

Synthesis of 5,10,15-trihexyl-10,15-dihydro-5*H*-diindolo[3,2-*a*:3',2'-*c*]carbazole: TAT(C_6)

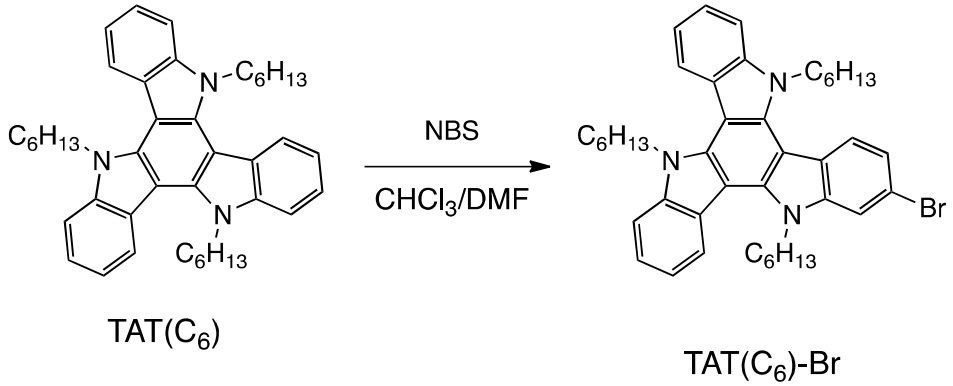

TAT(C_6) TAT(C_6)-Br

Synthesis of 2-bromo-5,10,15-trihexyl-10,15-dihydro-5*H*-diindolo[3,2-*a*:3',2'-*c*]carbazole: 2-BrTAT(C_6) (**2**)

Unambiguous structural determination of the synthetized regio-isomer.

Assessment of the nature of the regio-isomer has been unambiguously determined by proton NMR by preparing independently the 2-BrTAT (**2**) and the 3-BrTAT from their respective commercially available precursors (5-bromoisatin and 6-bromoisatin respectively, see **Figure S1** for details).

Direct bromination of unsubstituted TAT provided selectively the 2-BrTAT as deduced from the diagnostic proton signal **H1** at 7.71 ppm in $CDCl_3$ (see **Figure S3**). This results are in keeping with a recent publication where a HMQC NMR experiment has been used to confirm the structure of the obtained region-isomer.[S6] The 3-BrTAT compound exclusively prepared from the 6-bromoisatin (**Figure S1**) display a characteristic proton NMR signal at 8.33 ppm in $CDCl_3$ (see **Figure S7**).

a. Synthesis of 3-BrTAT

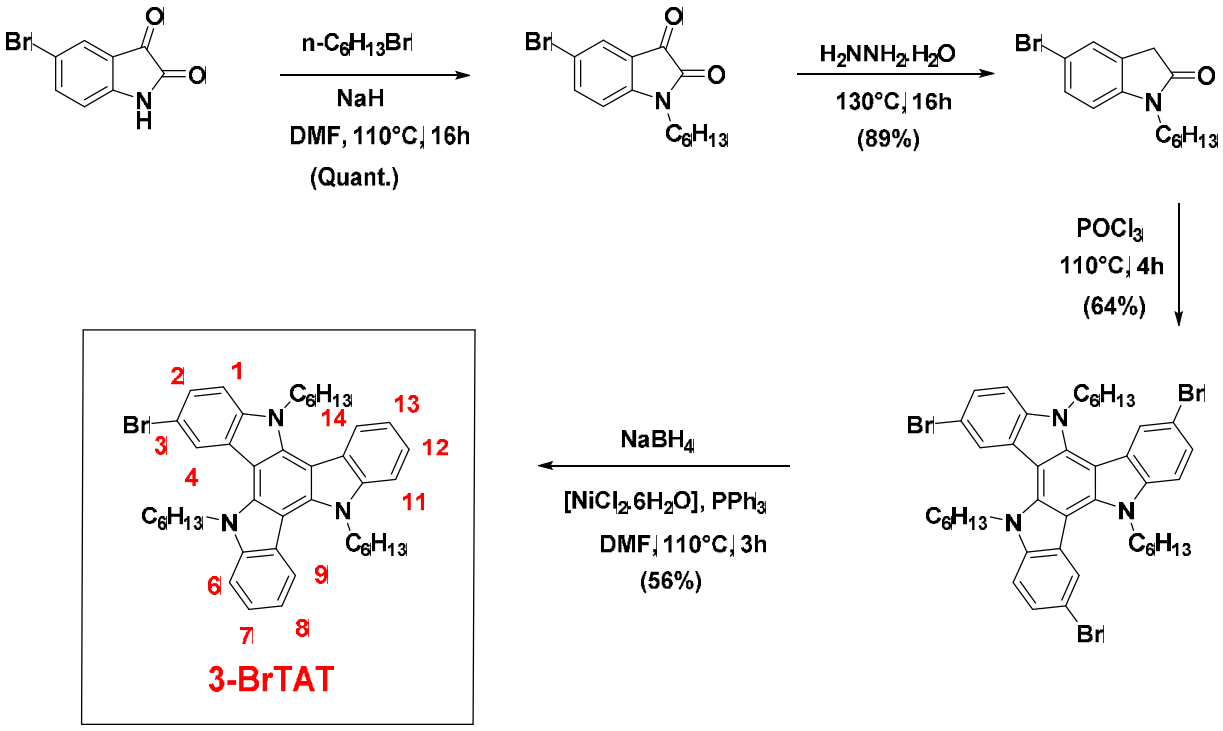

b. Synthesis of 2-BrTAT (2)

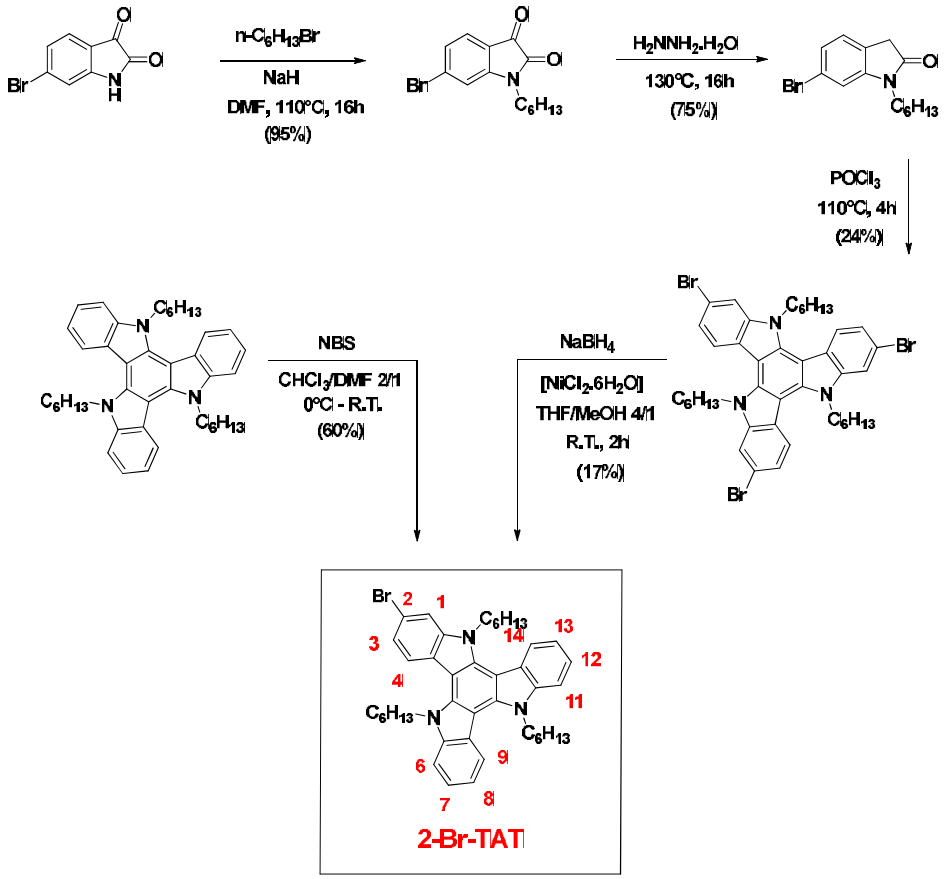

Figure S1. Synthetic pathways for the preparation of the two regioisomers.

NMR description

2-BrTAT (2): ^{1}H NMR (400 MHz, $CDCl_3$) δ (ppm) = 8.27 (d, 1H, ^{3}J = 8.1 Hz, **H9** or **H14**), 8.23 (d, 1H, ^{3}J = 8.1 Hz, **H9** or **H14**), 8.06 (dd, 1H, ^{3}J = 8.5 Hz, ^{4}J = 3.7 Hz, **H4**), 7.71 (s, 1H, **H1**), 7.62 (t, 2H, ^{3}J = 7.9 Hz, **H6** and **H11**), 7,46 (t, 2H, ^{3}J=7.1 Hz, **H7** and **H12**), 7.41 (d, 1H, ^{3}J = 9.0 Hz, **H3**), 7.35 (td, 2H, ^{3}J = 7.6 Hz, ^{4}J = 2.4 Hz, **H8** and **H13**), 4.74-4.84 (m, 4H), 4.84-4.90 (m, 2H), 1.88-2.03 (m, 6H), 1.20-1.33 (m, 18H), 0.77-0.86 (m, 9H). ^{13}C NMR (75 MHz, $CDCl_3$, 298 K): δ (ppm)= 142.0, 141.1, 139.1, 139.0, 138.6, 123.4, 123.3, 123.0, 122.61, 122.57, 122.5, 121.7, 121.61, 121.57, 119.9, 116.2, 113.4, 110.69, 110.68, 103.6, 103.2, 102.8, 47.19, 47.15, 47.09, 31.55, 31.53, 29.90, 29.85, 26.47, 26.40, 22.6, 14.0.

3-BrTAT: ^{1}H NMR (400 MHz, $CDCl_3$) δ (ppm) = 8.33 (d, 1H, ^{3}J = 1.2 Hz, **H4**), 8.25 (d, 1H, ^{3}J = 8.1 Hz, **H9** or **H14**), 8.21 (d, 1H, ^{3}J = 8.1 Hz, **H9** or **H14**), 7.62 (d, 1H, ^{3}J = 8.1 Hz, **H6** or **H11**), 7.61 (d, 1H, ^{3}J = 8.1 Hz, **H6** or **H11**), 7.5 (dd, 1H, ^{3}J = 8.7 Hz, ^{4}J = 1.2 Hz, **H2**), 7.46 (dd, 2H, ^{3}J = 7.8 Hz, **H7** and **H12**), 7.43 (d, 1H, ^{3}J = 8.7 Hz, **H1**), 7.34 (td, ^{3}J = 7.6 Hz, ^{4}J = 3.8 Hz, **H8** and **H13**), 4.84 (t, ^{3}J = 7.6 Hz), 4.80 (t, ^{3}J = 7.6 Hz), 4.73 (t, ^{3}J = 8.2 Hz), 2.06-2.15 (m, 2H), 1.93-2.01 (m, 2H), 1.84-1.93 (m, 2H), 1.43-1.53 (m, 2H), 1.20-1.43 (m, 16H), 7.41 (t, 3H, ^{3}J=7.1 Hz), 0.78-0.85 (m, 6H). ^{13}C NMR (75 MHz, $CDCl_3$, 298 K): δ (ppm)= 141.1, 140.9, 139.7, 139.4, 139.3, 138.4, 125.3, 125.2, 123.9, 123.4, 123.1, 123.0, 122.9, 121.6, 119.9, 119.8, 112.9, 111.8, 110.7, 110.3, 103.3, 103.0, 102.3, 47.19, 47.16, 47.14, 31.8, 31.54, 31.50, 30.6, 29.9, 29.7, 26.5, 26.45, 26.39, 22.8, 22.61, 22.57, 14.2, 14.05, 14.03.

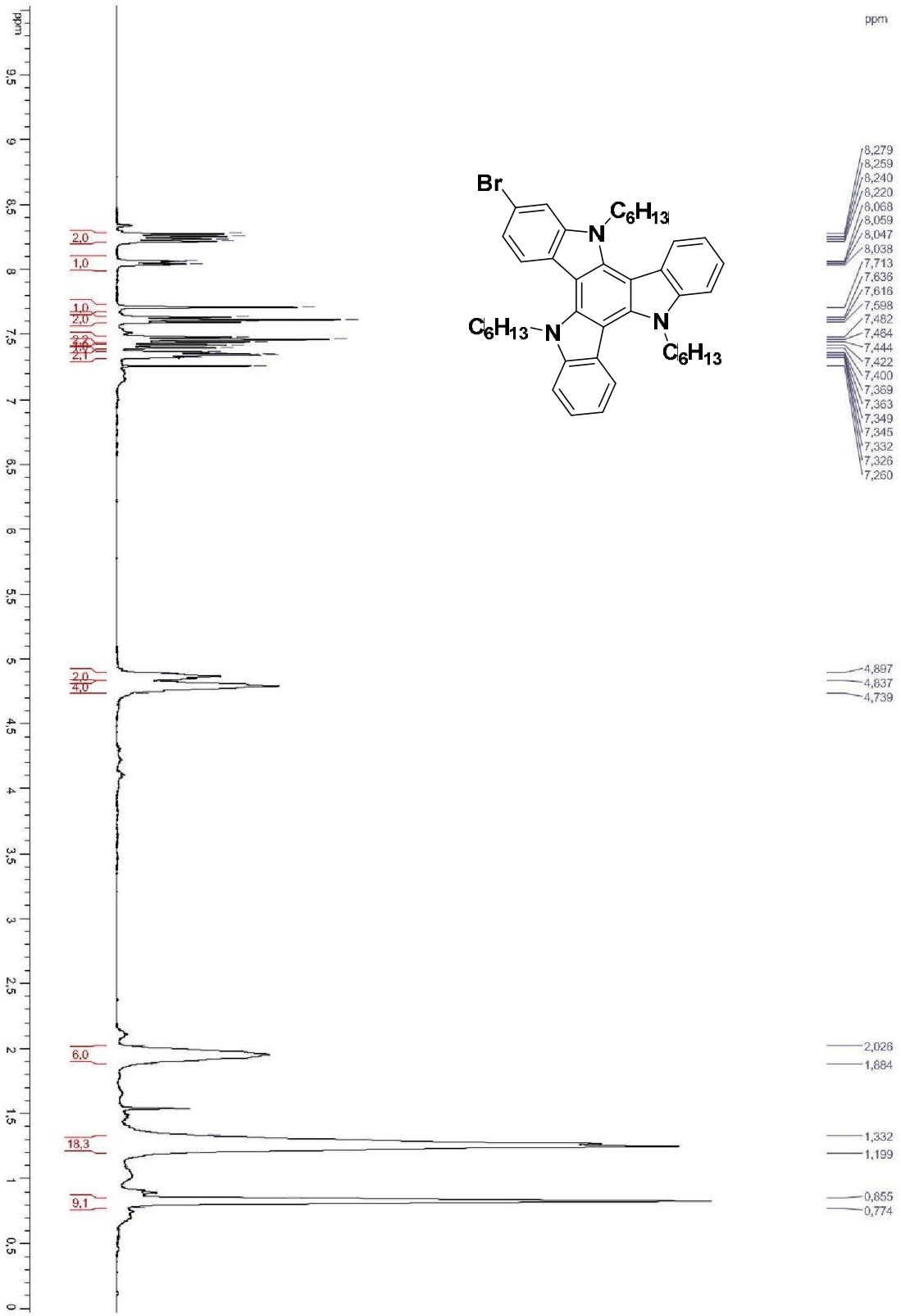

Figure S2. ^{1}H NMR spectrum of **2-BrTAT** ($CDCl_3$, 400 MHz, 298 K).

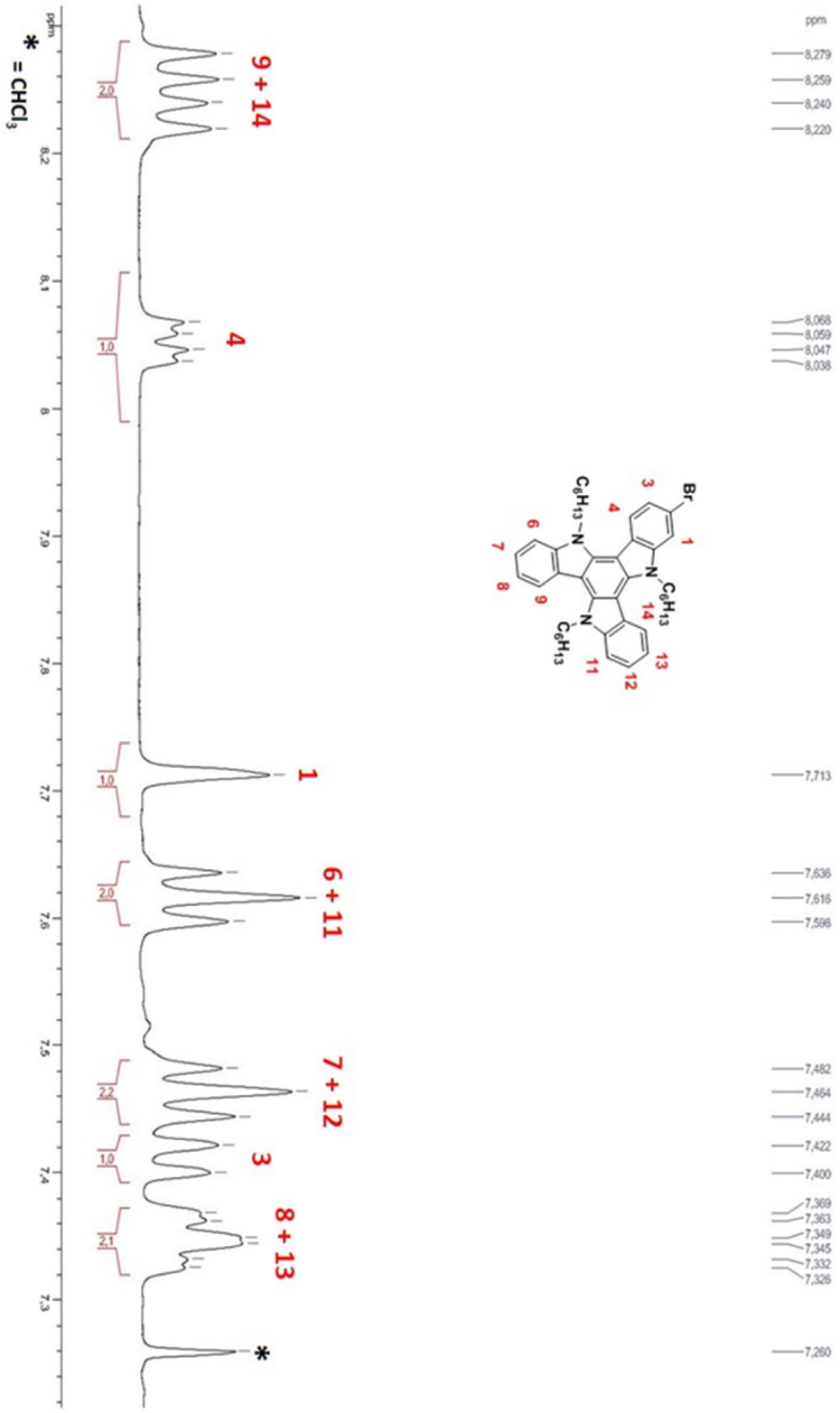

Figure S3. ^{1}H NMR spectrum (aromatic part) of **2-BrTAT** ($CDCl_3$, 400 MHz, 298 K).

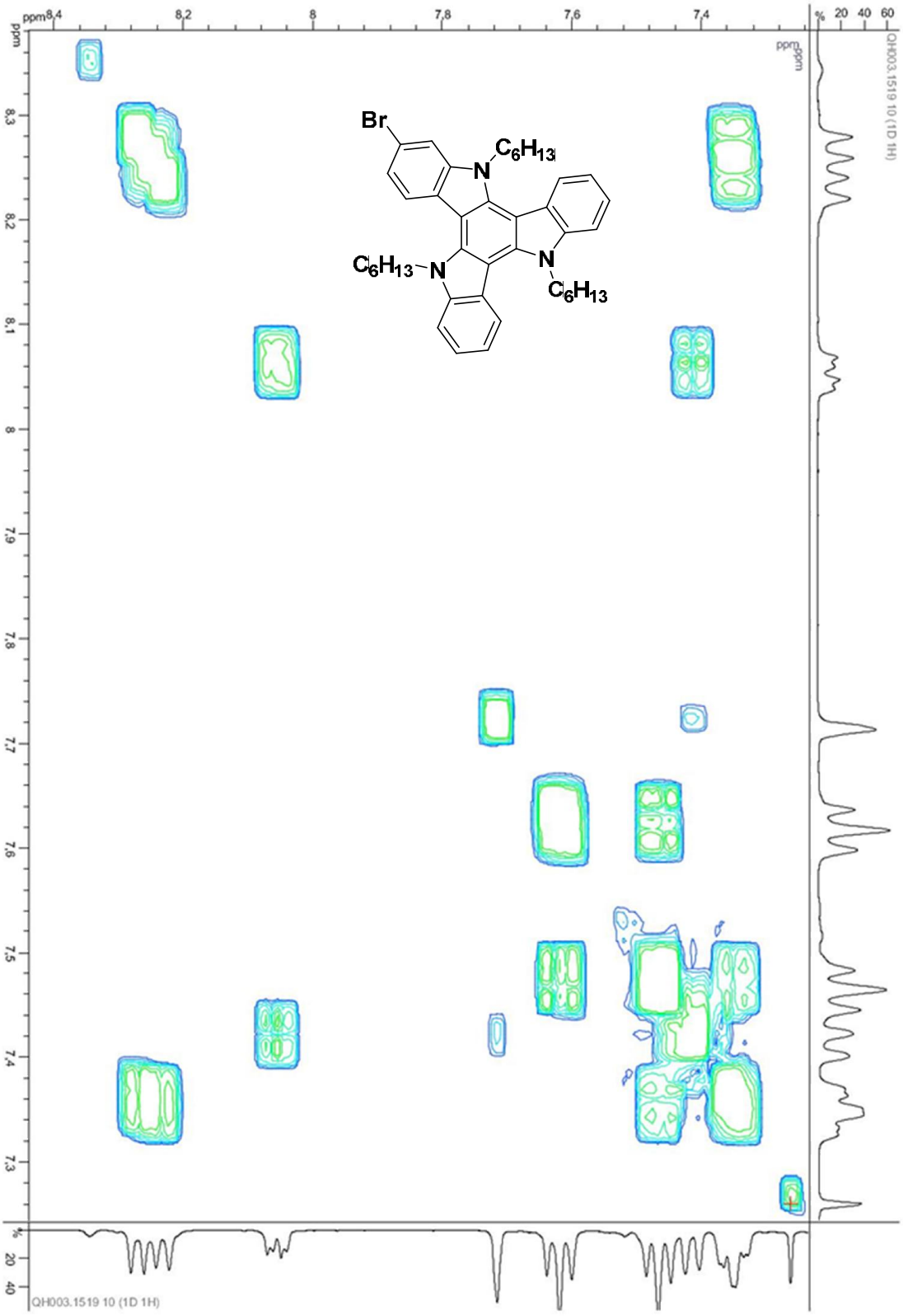

Figure S4. COSY NMR spectrum (aromatic part) of **2-BrTAT** ($CDCl_3$, 400 MHz, 298 K).

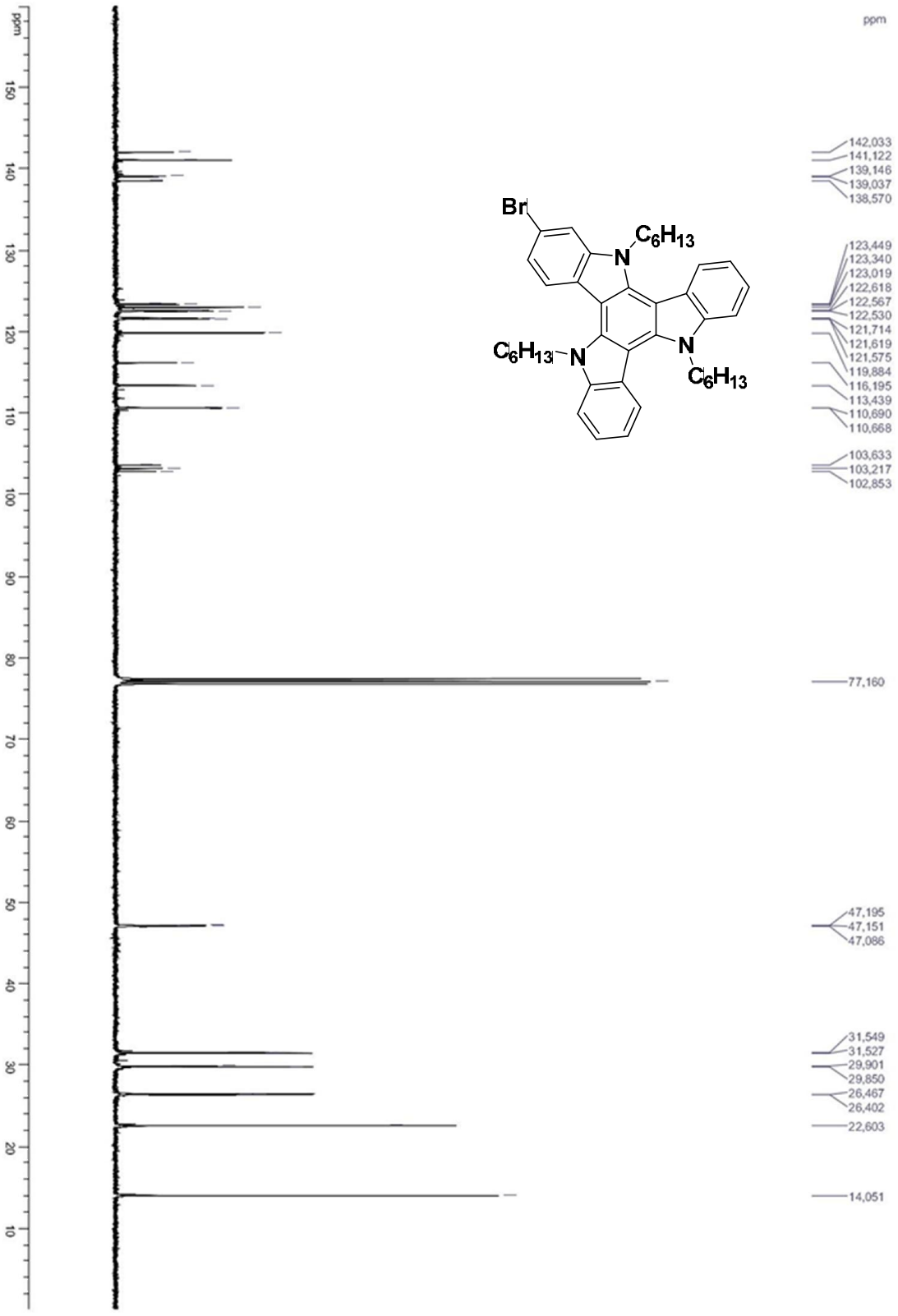

Figure S5. ^{13}C NMR spectrum of **2-BrTAT** ($CDCl_3$, 101 MHz, 298 K).

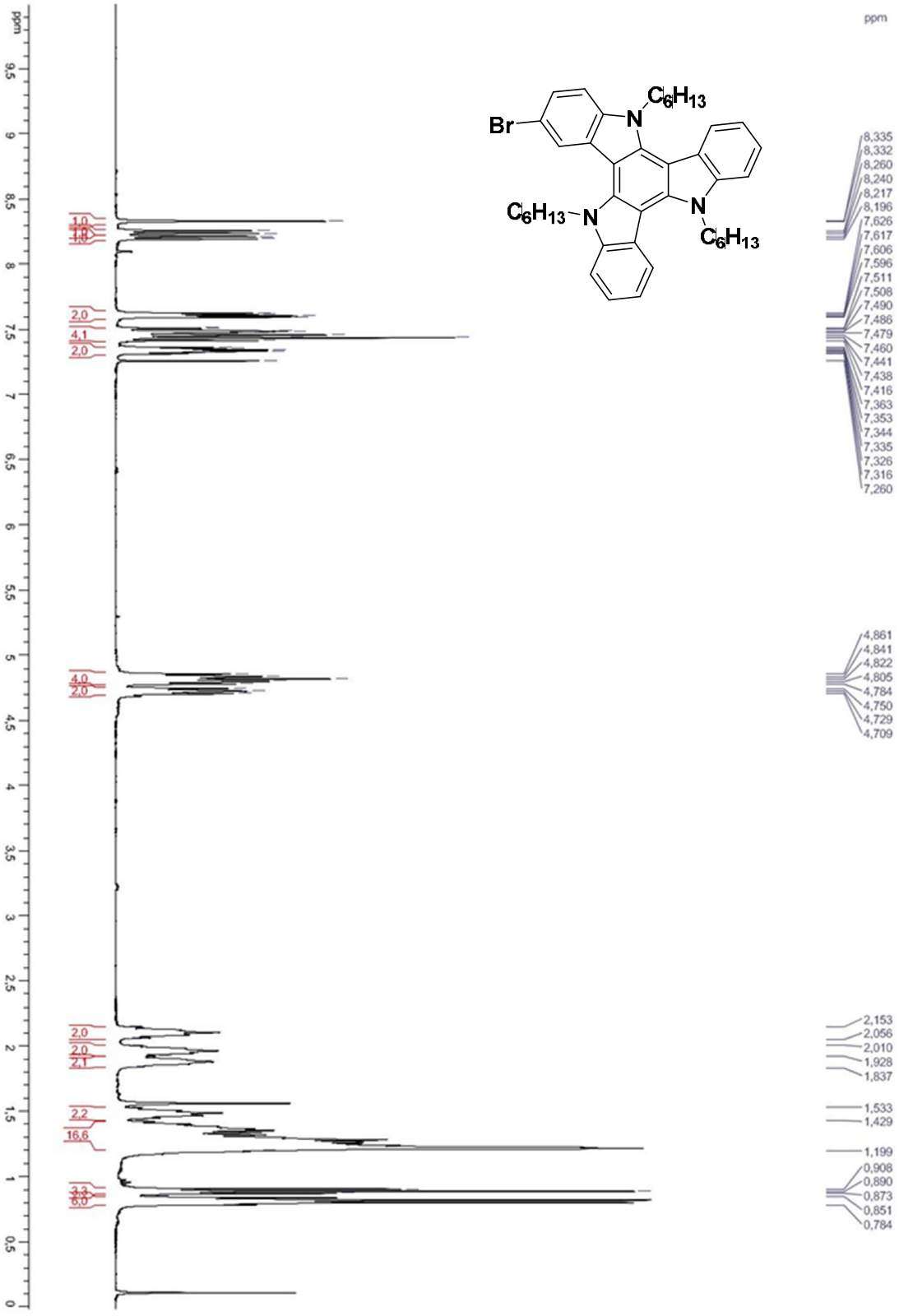

Figure S6. ^{1}H NMR spectrum of **3-BrTAT** ($CDCl_3$, 400 MHz, 298 K).

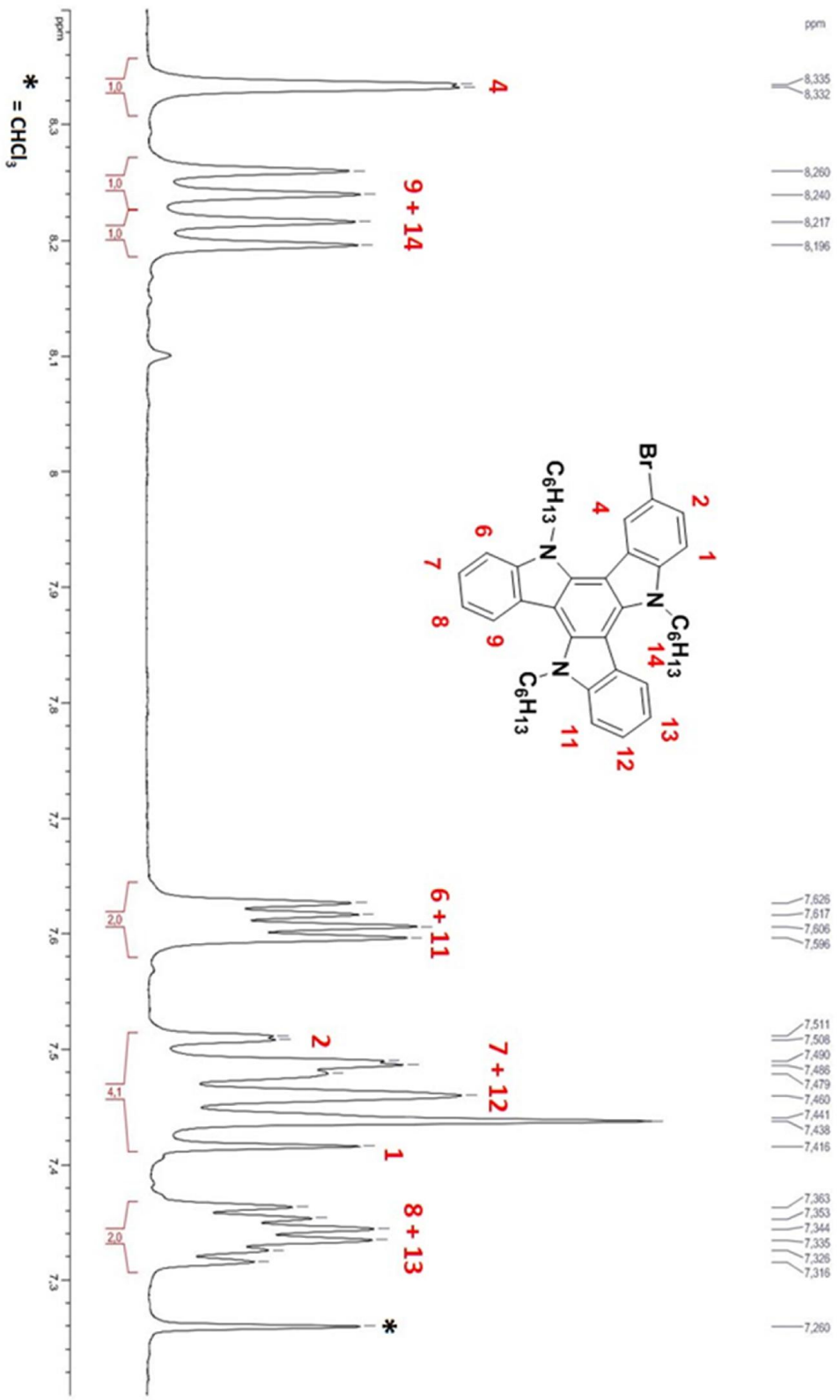

Figure S7. ^{1}H NMR spectrum (aromatic part) of **3-BrTAT** ($CDCl_3$, 400 MHz, 298 K).

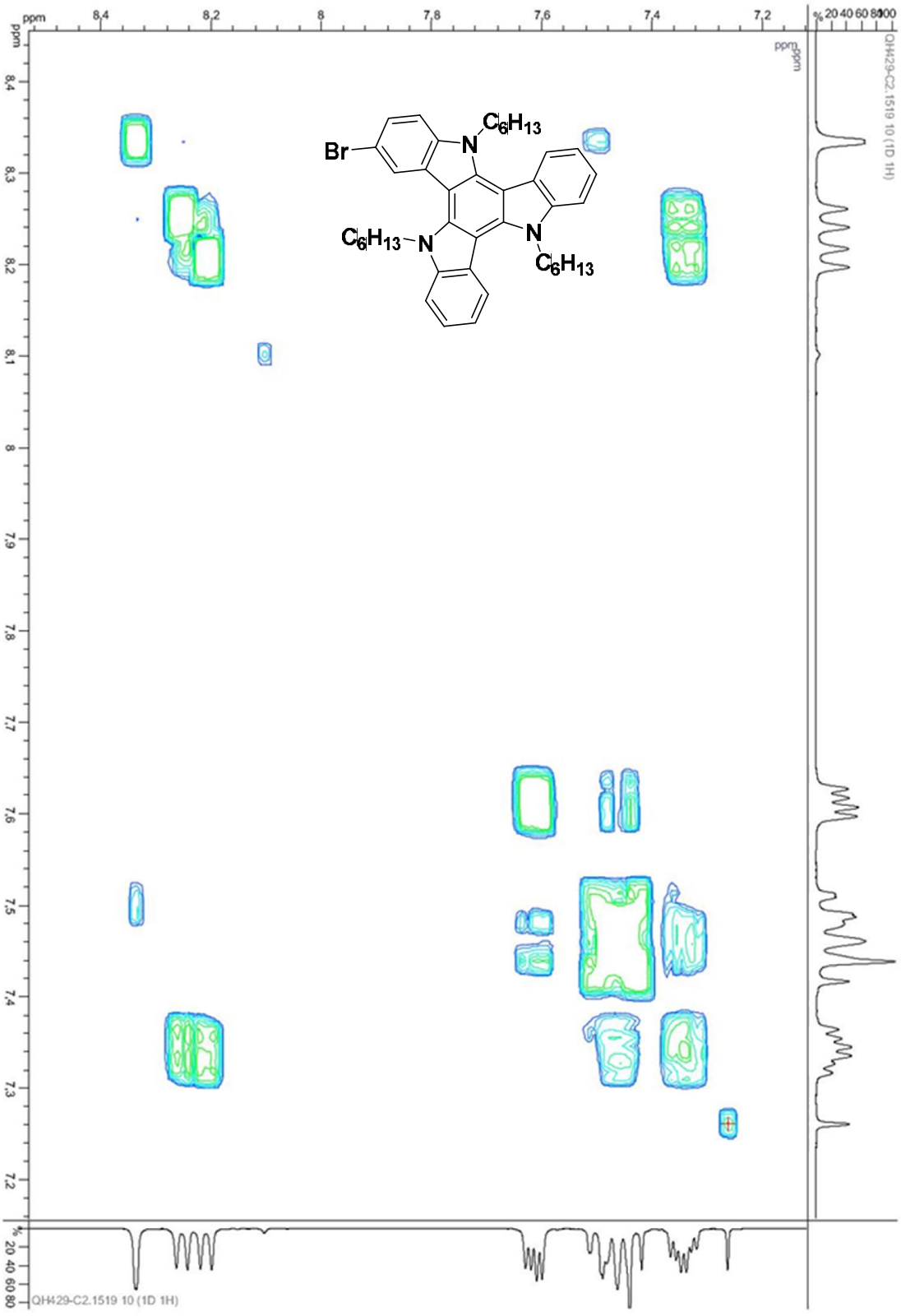

Figure S8. COSY NMR spectrum (aromatic part) of **3-BrTAT** ($CDCl_3$, 400 MHz, 298K).

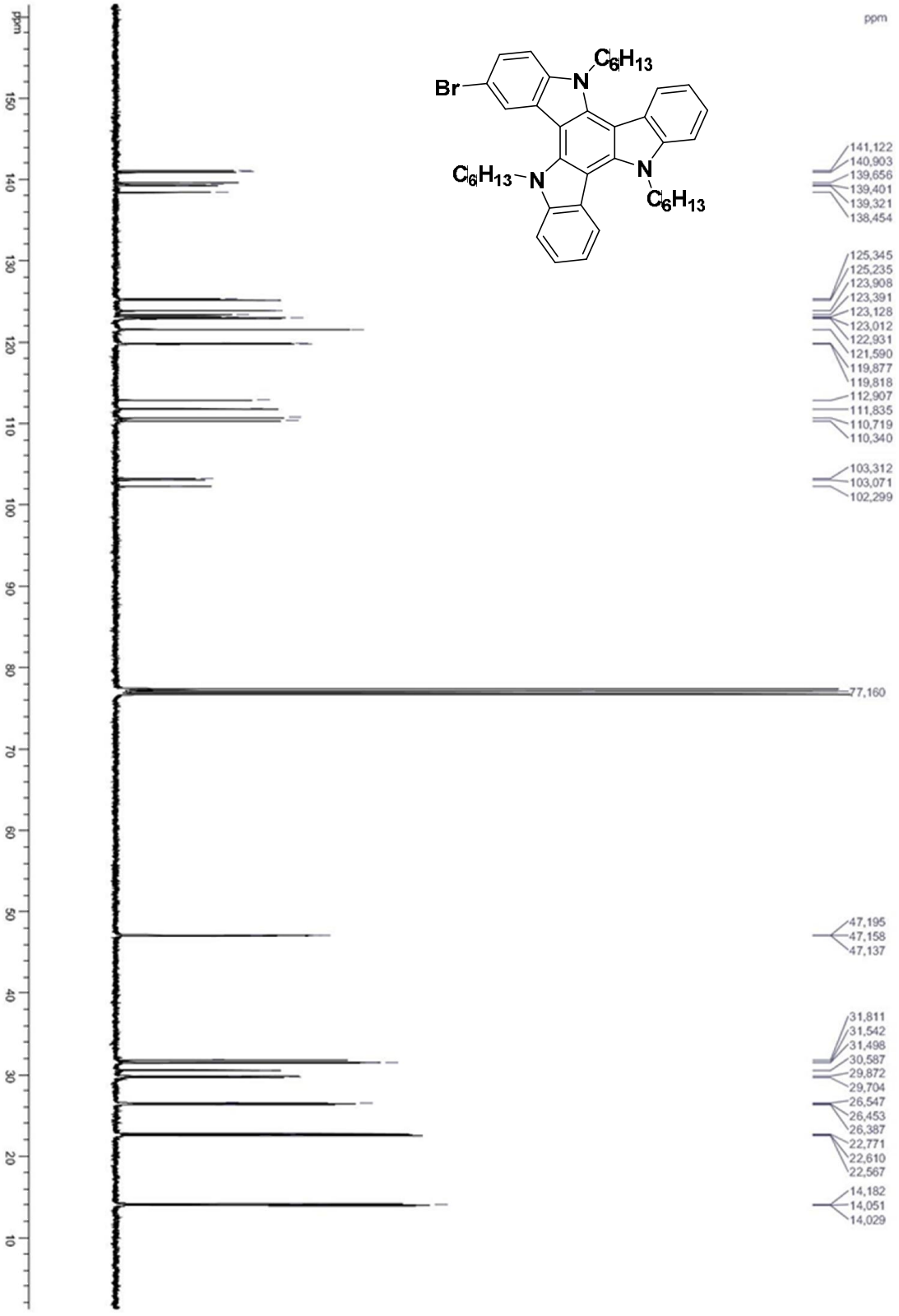

Figure S9. ^{13}C NMR spectrum of **3-BrTAT** ($CDCl_3$, 101 MHz, 298 K).

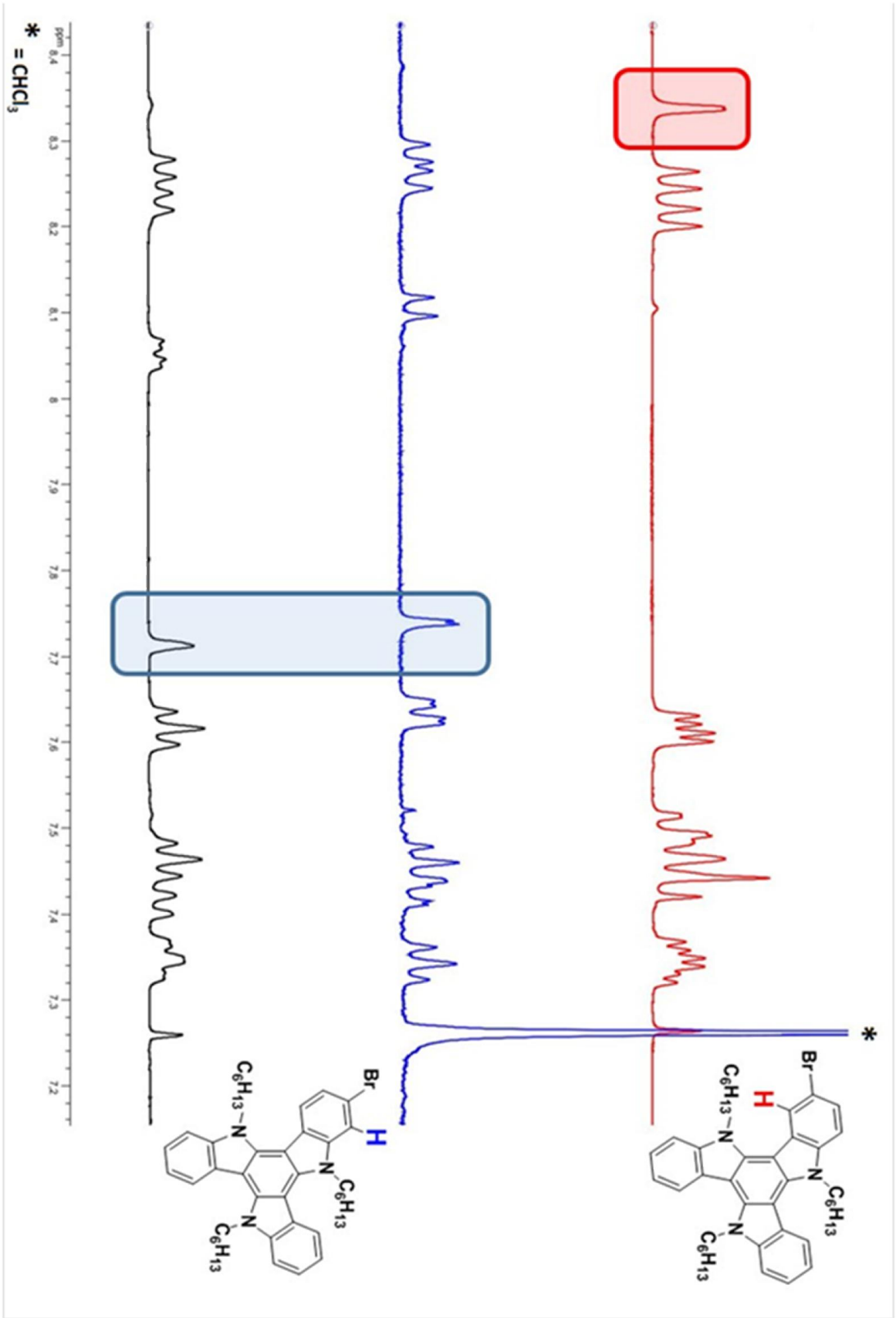

Figure S10. Superposition of ^{1}H NMR spectra of obtained products from Ni(0) catalyzed dehalogenation (black and red traces) and NBS bromination (blue trace) (in $CDCl_3$, 400 MHz, 298 K).

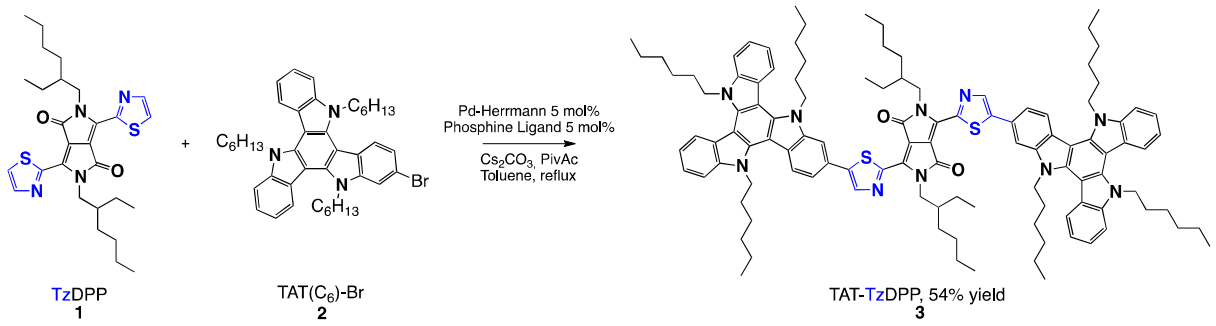

Synthesis of TAT-TzDPP by Pd-Catalyzed C-H Direct Arylation

2,5-bis(2-ethylhexyl)-3,6-bis(5-(5,10,15-trihexyl-10,15-dihydro-5*H*-diindolo[3,2-*a*:3',2'-*c*]carbazol-2-yl)thiazol-2-yl)pyrrolo[3,4-*c*]pyrrole-1,4(2*H*,5*H*)-dione : TAT-TzDPP (3)

NMR Traces

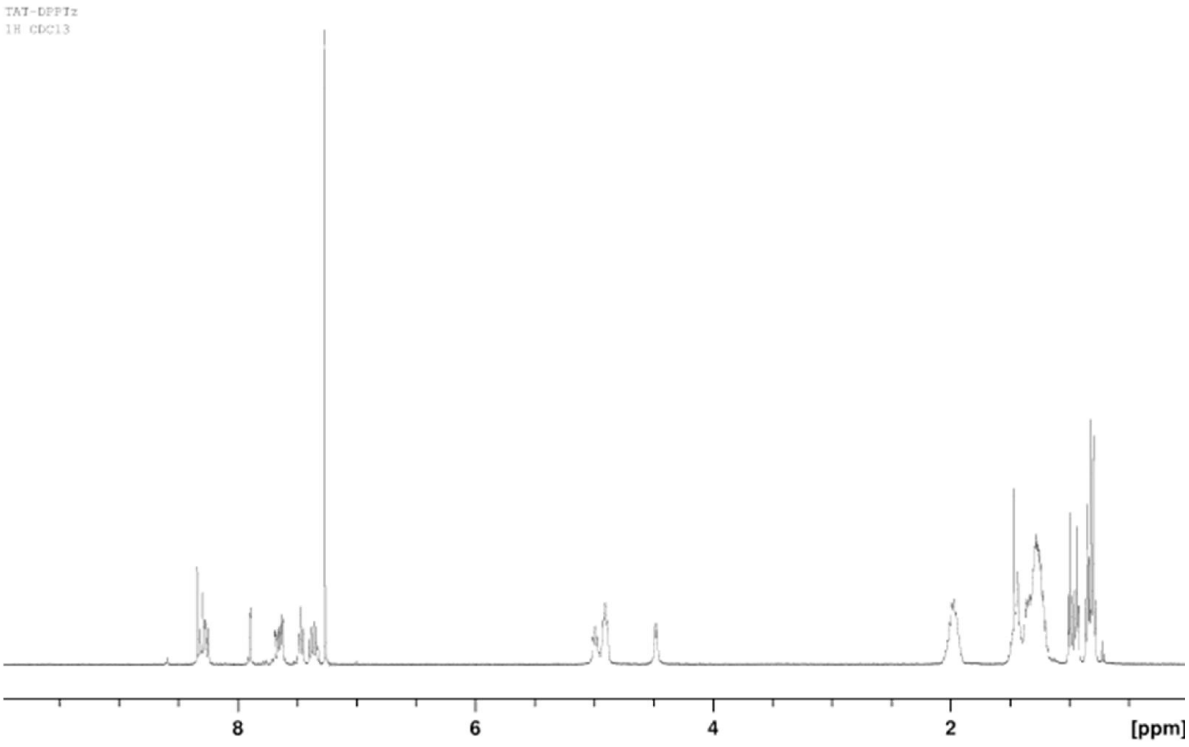

Figure S11. ^{1}H NMR of **TAT-TzDPP** in $CDCl_3$.

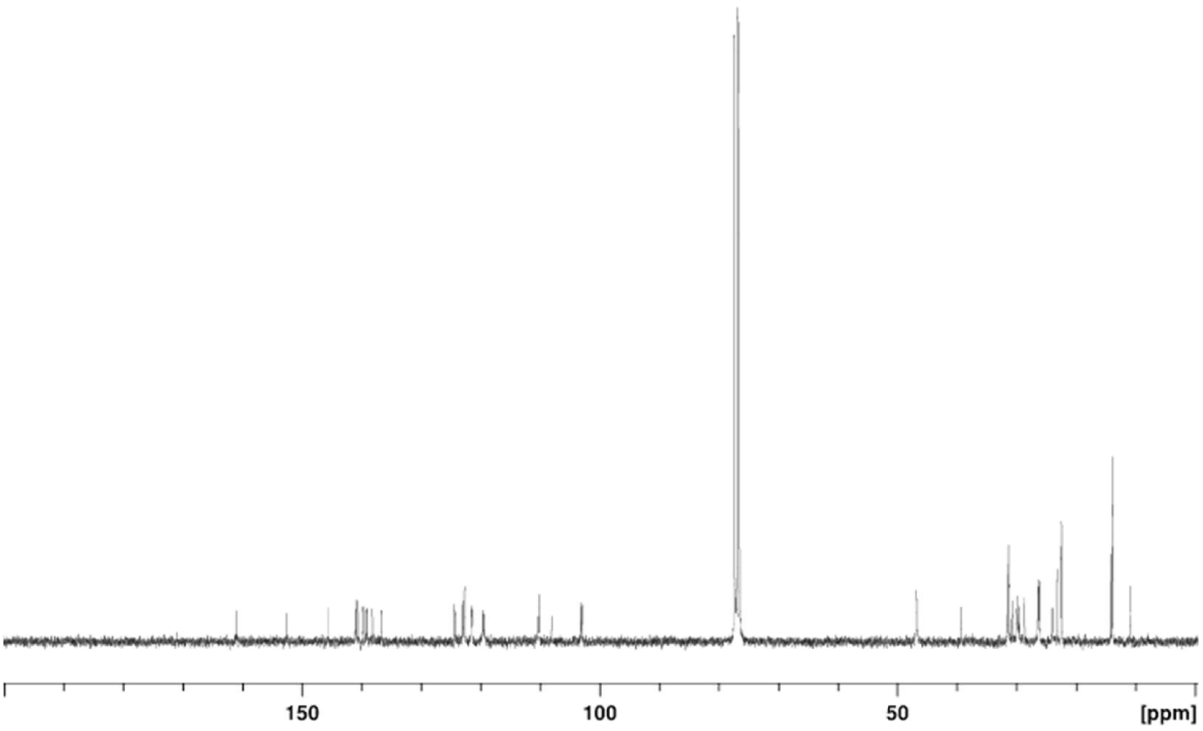

Figure S12. ^{13}C NMR of **TAT-TzDPP** in $CDCl_3$.

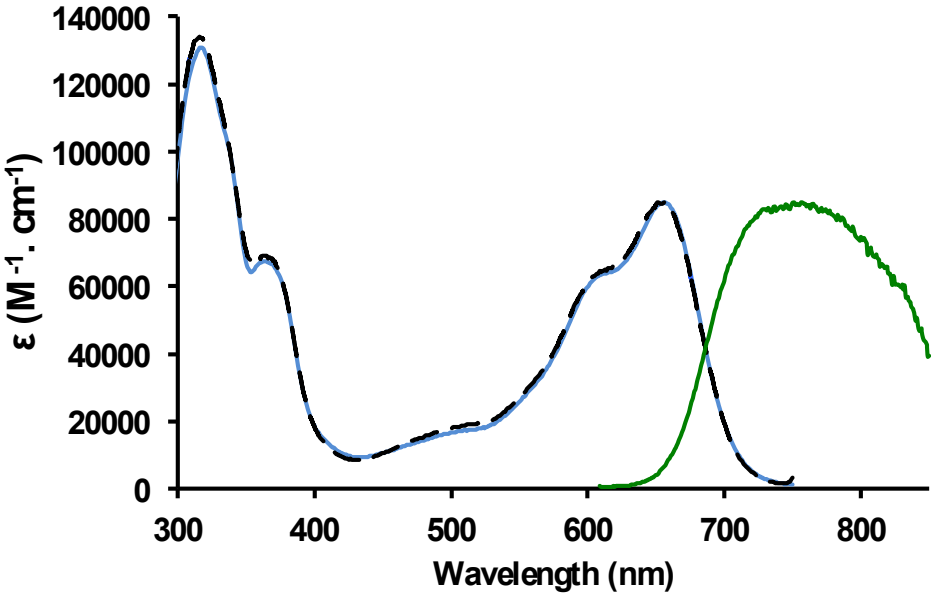

Figure S13. Absorption (blue trace), emission (green traces) and excitation (dashed lines) spectra in THF at room temperature for TAT-TzDPP.

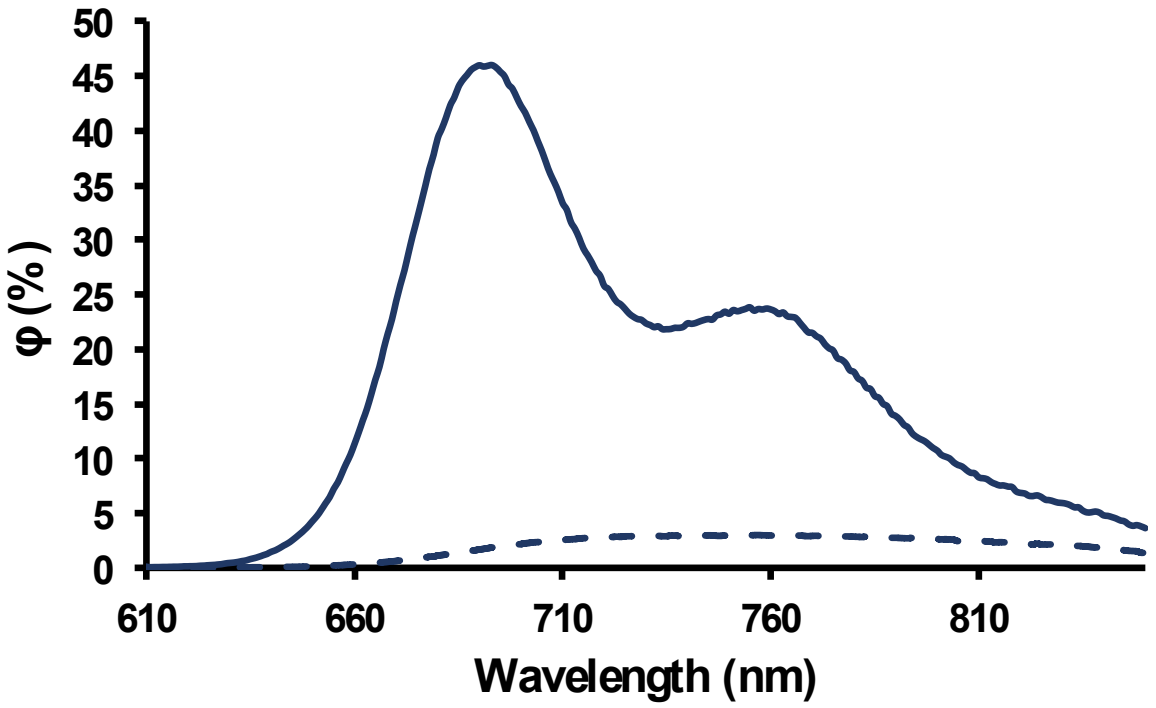

Figure S14. Emission profile measured in Toluene (full trace) and in THF (dashed trace) at room temperature for TAT-TzDPP

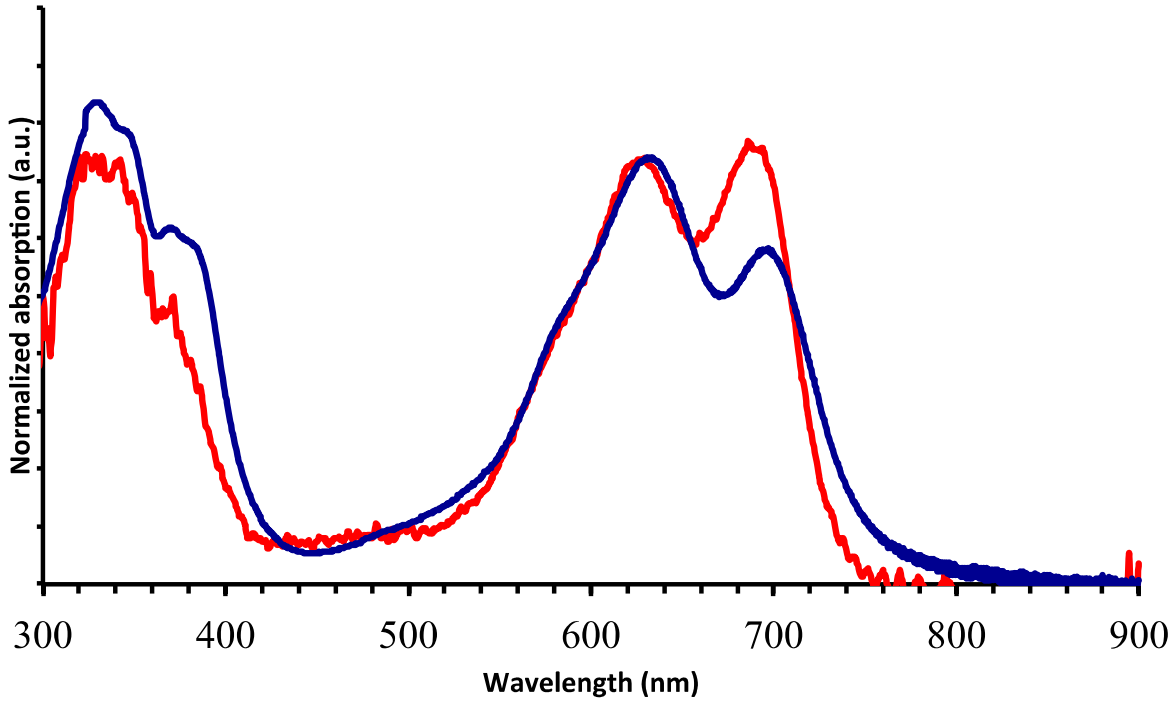

Figure S15. Solid state absorption spectra for TAT-TzDPP (blue line) and for TAT-ThDPP (red line).

Table S1. Selected redox potentials for TAT-TzDPP and TAT-ThDPP[S3] determined in dichloromethane solution at room temperature.[a)]

Compound	E_{Oxy}^0 V (ΔEp, mV)	E_{Red}^0 V (ΔEp, mV)	HOMO (eV)	LUMO (eV)	El_{gap} (eV)
TAT-TzDPP	+0.67 (70) ; +0.82 (124)** ; +1.16 (129)** ; +1.36 (80)	-0.93 (80) ; -1.49 (123)**	-5.45	-3.85	1.60
TAT-ThDPP[S3]			-5.31	-3.60	1.71

a) Tetrabutyl ammonium hexafluorophosphate was used as supporting electrolyte (0.1 M) and measurements were carried out under anhydrous nitrogen. *For irreversible processes E_{ap} or E_{cp} are quoted. ** bielectronic processes due to two overlapping waves.

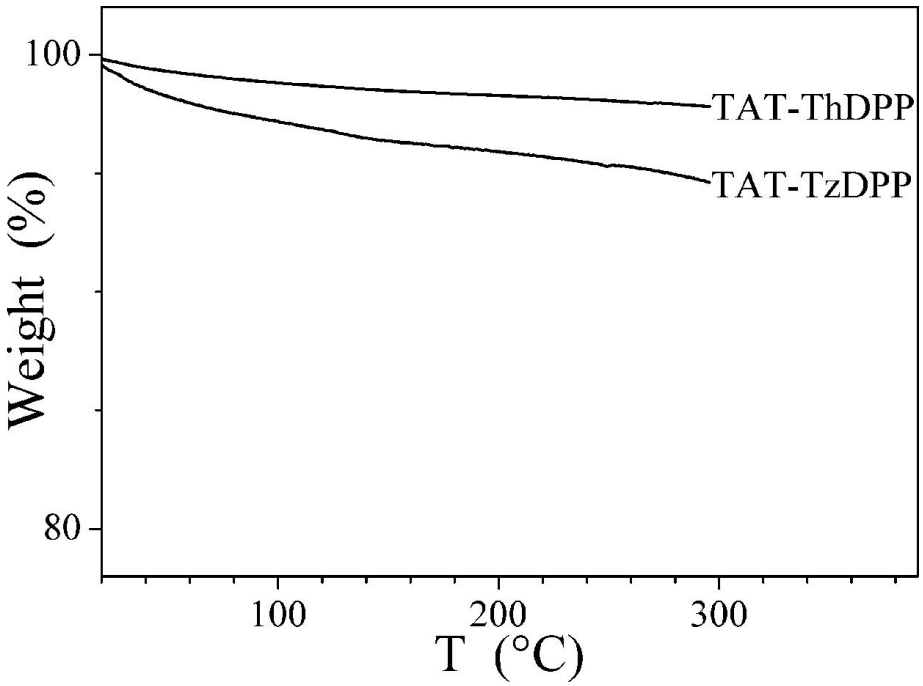

Figure S16. Thermogravimetric analyses of the two dyes (10°C/min, air). Curves show little weight loss below 300°C.

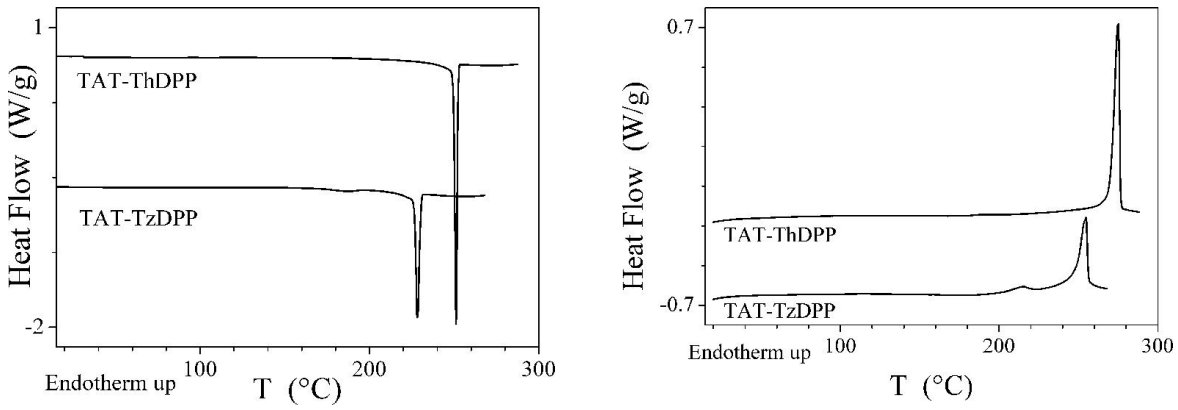

Figure S17. Second heating (left) and cooling (right) DSC traces at 5°C/min. The large peak corresponds to the transition to the isotropic liquid, occurring at 269°C (DH = 45 J/g) and 249°C (DH = 20 J/g), for TAT-ThDPP and TAT-TzDPP, respectively. DSC traces of TAT-TzDPP show an additional transition between mesophases around 220°C (DH = 4 J/g), which is not visible by POM and not reachable with SAXS equipment.

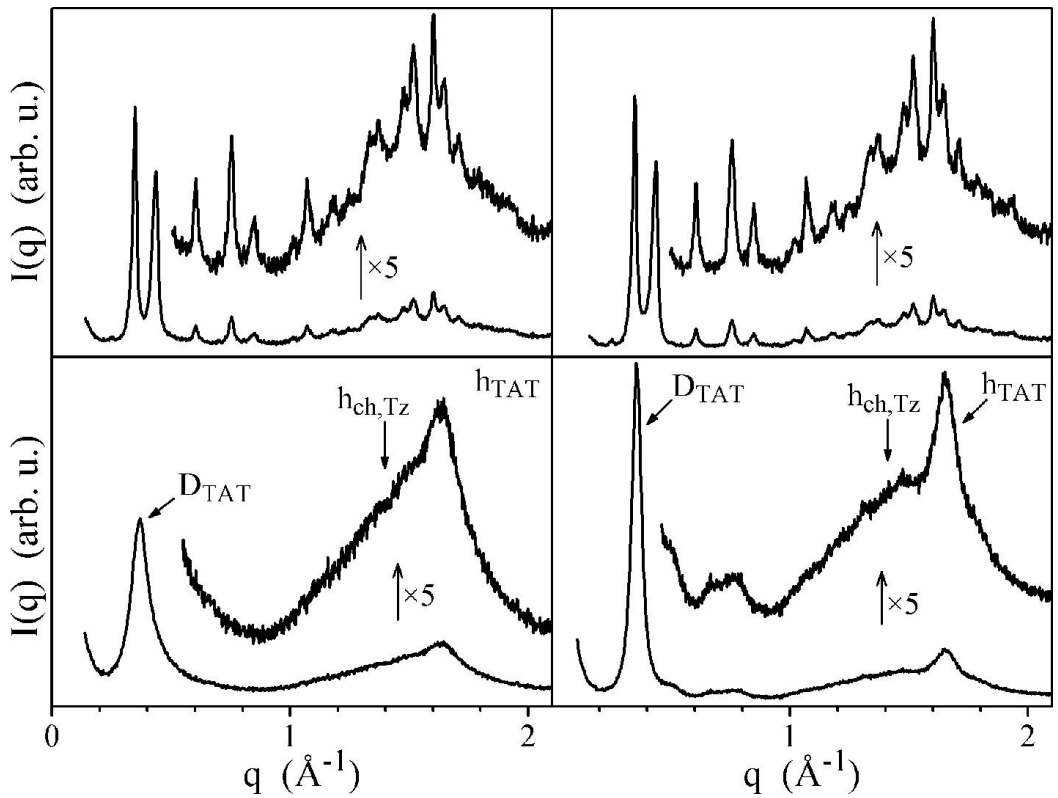

Figure S18: SAXS patterns of room temperature molecular organizations in the pristine state (left) and on cooling 110°C (right), of TAT-ThDPP (top) and TAT-TzDPP (bottom).

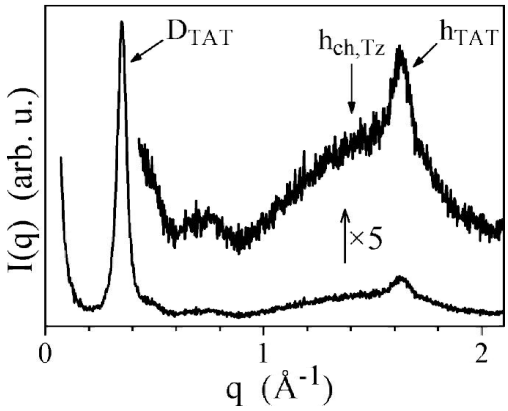

Figure S19: SAXS pattern of TAT-TzDPP at 110°C.

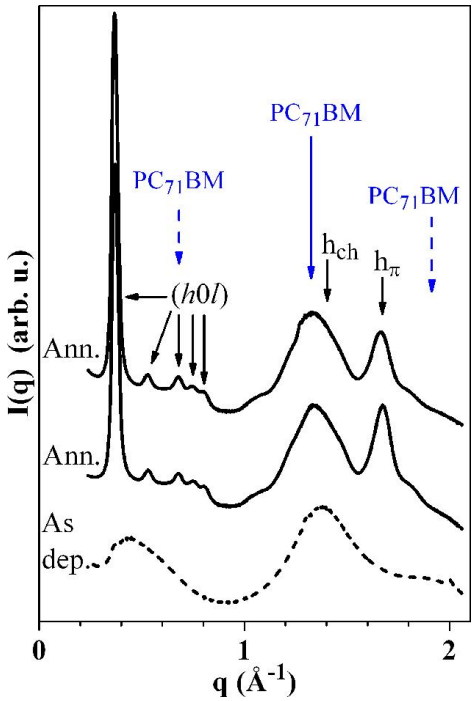

Figure S20: Radial profiles of GIWAXS patterns of TAT-TzDPP, as prepared (bottom) and annealed at 120°C for 10 min (middle), and of a blend TAT-TzDPP:$PC_{71}BM$ (ratio of 1:0.75) annealed in same conditions (top).

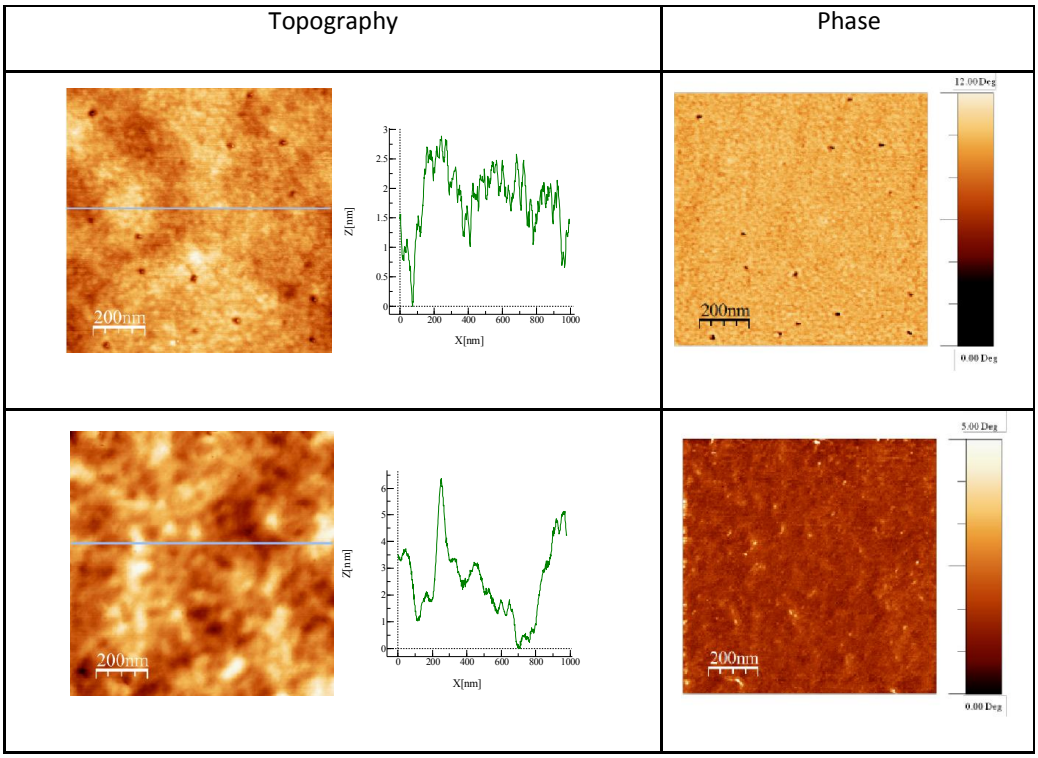

Figure S21. AFM topography image (left) with corresponding profile and phase image (right) of a film of TAT-TzDPP:$PC_{71}BM$ processed in $CHCl_3$ before (top) and after (bottom) thermal annealing (10 minutes at 120°C).

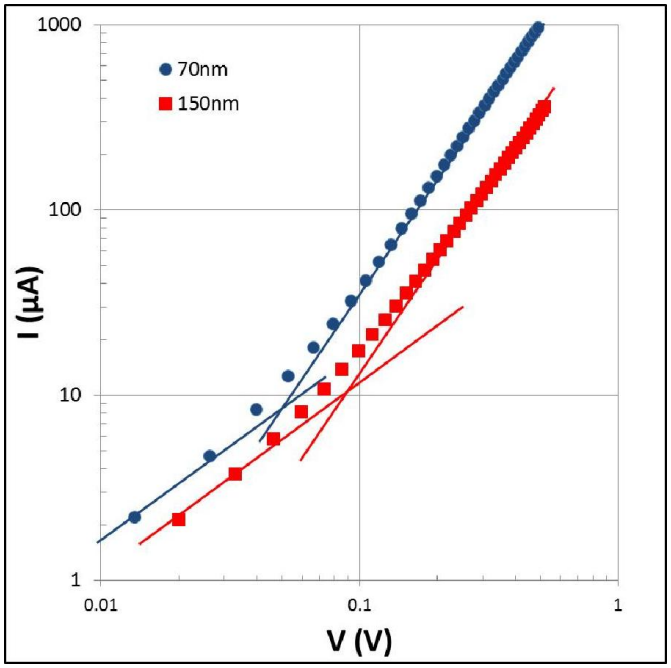

Figure S22. (I-V) characteristics for hole-only TAT-TzDPP devices with different thicknesses. The lines corresponds to a power-law dependence with a slope of one (Ohm regime) or two (SCLC regime).

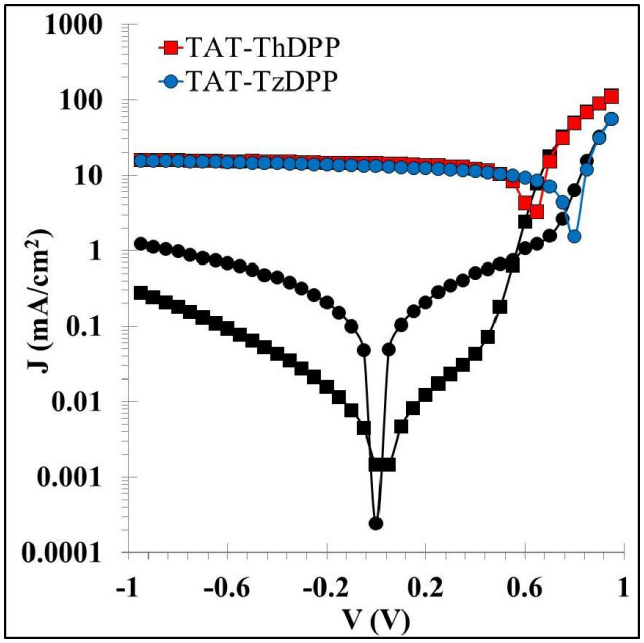

Figure S23. (J-V) curves in a semi-log scale obtained in the dark (black symbols) and under standard AM1.5G (100 mW/cm^2) illumination conditions (colored symbols). The squares correspond to the TAT-ThDPP compound (standard architecture) and the circles to the TAT-TzDPP compound (inverted architecture).

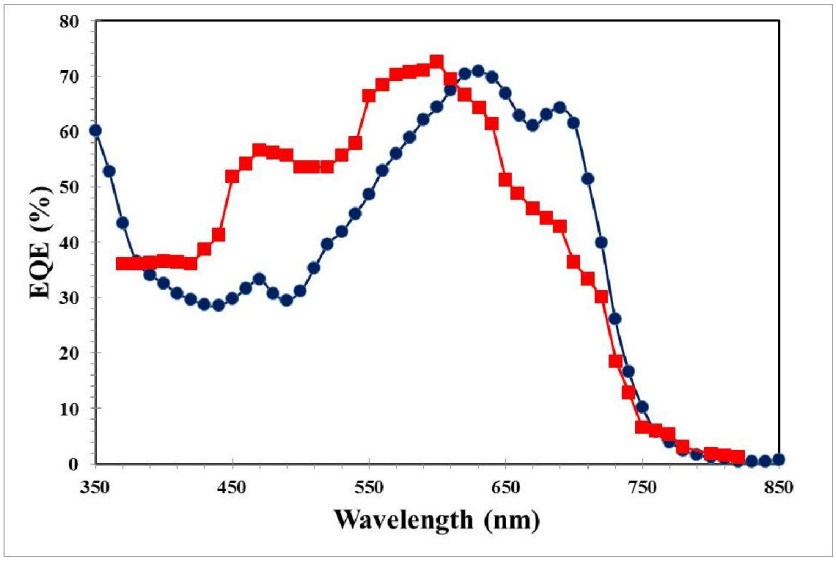

Figure S24. External quantum efficiency (EQE) measured on an inverted TAT-TzDPP based device (blue circles) and on a standard TAT-ThDPP based device (red squares). The calculated J_{sc} from the EQE spectra were 11.3 and 12 mA/cm^2 for TAT-TzDPP and TAT-ThDPP, respectively. The measured J_{sc} on the same devices under standard AM1.5G (100 mW/cm^2) illumination were 11.9 and 12.5 mA/cm^2 for TAT-TzDPP and TAT-ThDPP, respectively.

In order to determine possible efficiency limiting factors in TAT-TzDPP based devices, we performed additional photovoltaic measurements using neutral density filters to change the incident light power from 0.45 to 100 mW.cm^{-2}. The short circuit current density (J_{sc}) was observed to depend almost linearly on the light power (Figure S25). This is a strong evidence of a device either with negligible recombination or where mostly monomolecular single-body recombination i.e. by geminate recombination occurs.[S4] The high EQE values measured (more than 70% at 630 nm) tends to favour the first hypothesis i.e. a device where most of the absorbed photons leads to the collection of free charge carriers.

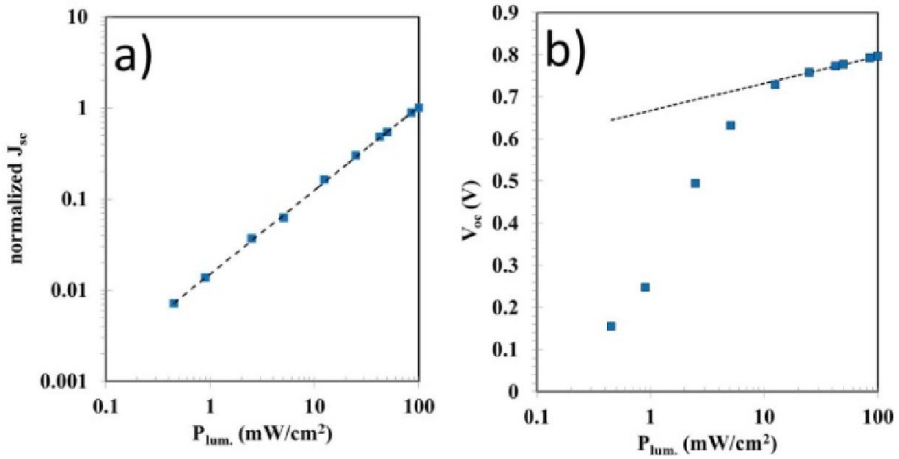

Figure S25. (a) Normalized J_{sc} as a function of the incident light power for a TAT-TzDPP based device (symbols). The dotted line corresponds to a power law fit following the equation: $J_{sc} \alpha P_{lum.}^{0.92}$. (b) V_{oc} as a function of the incident light power for the same device. The dotted line corresponds to a V_{oc} with a logarithmic dependence on light power with a slope of kT/q as expected in a cell where only bimolecular recombination occurs.

On the other hand, in a device with negligible leakage current and where only bimolecular recombination occurs, the open circuit voltage V_{oc} is expected to follow the equation:

$$V_{oc} = \frac{E_g}{q} - \frac{kT}{q} Ln\left(\frac{(1-P)\gamma N_c^2}{PG}\right) \quad (1)$$

where E_g is the band gap, q is the elementary charge, k is Boltzmann's constant, T is temperature, P is the dissociation probability of a bound electron-hole pair, g is the bimolecular recombination rate coefficient, N_c is the effective density of states, and G is the photogeneration rate. G is the only term in Eq. (1) that depends on light power.[S5]

Therefore, a system with only bimolecular recombination will exhibit a V_{oc} with a logarithmic dependence on light power with a slope of kT/q. as shown by the dotted line in Figure S25. At low light intensity, V_{oc} deviates from equation (1) as the assumption of a negligible leakage current is no longer valid in our cells for a light intensity below 10 mW/cm^2.

Finally, under short-circuit conditions, the charge carrier collection is sufficient to avoid charge recombination while under open-circuit conditions, bimolecular recombination dominates.

Supplementary References

[S1**]** B. Carsten, J.M. Szarko, L. Lu, H.J. Son, F. He, Y.Y Botros, L.X. Chen and L. Yu, *Macromolecules*, 2012, **45**, 6390.

[S2**]** W.A. Herrmann, C. Brossmer, K. Öfele, C.-P. Reisinger, T. Priermeier, M. Beller and H. Fischer, *Angew. Chem. Int. Ed. Engl*., 1995, **34**, 1844.

[S3**]** T. Bura, N. Leclerc, R. Bechara, P. Lévêque, T. Heiser and R. Ziessel, *Adv. Energy Mater.*, 2013, ***3***, 1118.

[S4**]** C.M. Proctor, M. Kuik and T.-Q Nguyen, *Prog. Polym. Sci.*, 2013, **38**, 1941.

[S5**]** L.J.A. Koster, V.D Mihailetchi, R. Ramaker and P.W.M. Blom, *Appl. Phys. Lett.*, 2005, **86**, 123509.

[S6**]** C. Ruiz, J.T. López Navarrete, M. Carmen Ruiz Delgado and B. Gómez-Lor B. *Org. Lett.*, *2*015, **17**, 2258.